# https://doi.org/10.1017/jfm.2017.155 Published online by Cambridge University Press

# JFM RAPIDS journals.cambridge.org/rapids



# Transitional behaviour of convective patterns in free convection in porous media

Hamid Karani<sup>1,†</sup> and Christian Huber<sup>2</sup>

(Received 5 January 2017; revised 7 March 2017; accepted 8 March 2017; first published online 6 April 2017)

The present study focuses on the transition between steady convective patterns in fluid-saturated porous media. We conduct experiments to identify the transition point from the single- to double-cell pattern in a two-dimensional porous medium. We then perform a basin stability analysis to assess the relative stability of different convective modes. The resulting basin stability diagram not only provides the domains of coexistence of different modes, but it also shows that the likelihood of finding convective patterns depends strongly on the Rayleigh number. The experimentally observed transition point from single- to double-cell mode agrees well with the stochastically preferred mode inferred from the basin stability diagram.

**Key words:** bifurcation, convection in porous media, convective instability

### 1. Introduction

The emergence of flow patterns is omnipresent in nature and is observed in numerous hydrodynamical systems such as thermal convection, convection in binary mixtures, surface waves, rotating fluids and Taylor–Couette flow (Cross & Hohenberg 1993). The problem of free convection in a fluid-saturated porous medium subjected to an adverse temperature gradient, which is known as Horton–Rogers–Lapwood convection (HRLC), is an example of a dynamical system showing a multiplicity of flow patterns (Horne 1979; Schubert & Straus 1979; Straus & Schubert 1979; Steen 1983; Riley & Winters 1989; Sezai 2005; Henry *et al.* 2012). HRLC was first studied by Horton & Rogers (1945) and Lapwood (1948), who performed linear stability analysis aimed at identifying the critical conditions for the onset of convection in a horizontally infinite porous layer. Beck (1972) extended the linear stability analysis of these pioneering studies to confined porous enclosures. Several numerical studies

†Email address for correspondence: hamid.karani@gatech.edu

<sup>&</sup>lt;sup>1</sup>School of Earth and Atmospheric Sciences, Georgia Institute of Technology, Atlanta, GA 30332-03403, USA

<sup>&</sup>lt;sup>2</sup>Department of Earth, Environmental and Planetary Sciences, Brown University, Providence, RI 02912, USA

later confirmed the multiplicity of convection solutions (Horne 1979; Schubert & Straus 1979; Straus & Schubert 1979) at supercritical values of the Rayleigh number. The results showed that, depending on the initial perturbation, different convection patterns can occur and remain stable at a given Rayleigh number. A significant research activity has followed to identify these multiple convection solutions in HRLC (Steen 1983; Riley & Winters 1989; Sezai 2005; Henry *et al.* 2012). The bifurcation analysis of Riley & Winters (1989) is one of the first systematic studies to characterize the different convection modes in a two-dimensional (2-D) saturated porous cavity using methods developed for dynamical system theory. Recently, Henry *et al.* (2012) extended this work using a continuation technique to track the first four stable convection modes from the steady bifurcation point up to the corresponding oscillatory (Hopf) bifurcation point of each mode.

The standard bifurcation analysis of HRLC using linear stability analysis and continuation techniques is based on the assumption that the system is subjected to infinitesimal perturbations. These techniques enable the detection of bifurcation points and smoothly track each stable convection mode over a range of Rayleigh number. The main drawback, however, is that they only provide local information about the (range of) existence and any possible coexistence of different convection modes. It is now well understood that multistable dynamical systems exhibit complex interactions, such as transition and switching between the dominant states. Therefore, knowing the local information about their existence provides only a partial understanding of the overall behaviour of a multistable system (Feudel 2008; Zhou *et al.* 2012).

The main idea of the current study is to apply a new approach for HRLC, which not only provides the local information about the (co)existence of different patterns, but also determines their relative stability as well as how the basin stability of these modes contracts or expands as the Rayleigh number varies. The strategy we are adopting here is first to provide new experimental evidence on the transition from a single-cell to double-cell convection mode in a 2-D HRLC problem. The transition happens at a Rayleigh number at which the two modes can coexist as stable patterns, according to bifurcation analysis. In order to explain the observed modal transition, we perform a basin stability analysis (Menck *et al.* 2013) on 2-D HRLC. Menck *et al.* (2013) showed how, in a multistable dynamical system, the volume of an attractor's basin provides a universal measure for quantifying the degree of stability of a state to random perturbations. Thus, in addition to identifying the range of existence of each mode, the resulting basin stability diagram carries information about how the likelihood of finding each mode varies with the Rayleigh number – a dynamical characteristic of HRLC that cannot be inferred from bifurcation diagrams.

The paper is organized as follows: the mathematical formulation of the HRLC problem is introduced in § 2. Details on the experimental set-up and the corresponding experimental results bearing on the transition between modes are presented in § 3. We develop a basin stability analysis for HRLC in § 4.

### 2. Mathematical formulation

For an isotropic porous medium subjected to a uniform cold temperature  $T_C$  from the top boundary and hot temperature  $T_H$  from the bottom surface, we choose H,  $\alpha_m/H$ ,  $H^2/\alpha_m$  and  $\theta = (T-T_C)/(T_H-T_C)$  as the dimensionless variables for length, velocity, time and temperature, respectively, where H is the height of the porous layer, and  $\alpha_m = k_m/(\rho c)_f$  is the effective diffusivity of the medium based on the stagnant thermal conductivity  $k_m$  and fluid heat capacitance  $(\rho c)_f$ . The momentum

and energy conservation equations take the following dimensionless form in terms of the stream function  $\psi$  (Nield & Bejan 2013):

$$\nabla^2 \psi = Ra \, \frac{\partial \theta}{\partial x},\tag{2.1}$$

$$\frac{\partial \theta}{\partial t} + V \cdot \nabla \theta = \nabla^2 \theta, \tag{2.2}$$

where  $V = (u, v) = (-\partial \psi / \partial y, \partial \psi / \partial x)$  and Ra is the Rayleigh number defined as

$$Ra = \frac{g\beta(T_H - T_C)KH}{\alpha_m \nu_f},\tag{2.3}$$

where K is the isotropic permeability of the medium,  $v_f$  is the kinematic viscosity of the fluid,  $\beta$  is the thermal expansion coefficient and g is the gravitational acceleration. The appropriate boundary conditions are constant temperature and zero flux for the horizontal and vertical surfaces, respectively, while a no-slip condition is applied at the surface of the solid:

$$\psi = 0$$
,  $\theta = 1$ , for  $y = 0$ , for all  $x$ , (2.4 $a$ , $b$ )

$$\psi = 0$$
,  $\theta = 0$ , for  $y = 1$ , for all  $x$ , (2.5 $a$ , $b$ )

$$\psi = 0$$
,  $\frac{\partial \theta}{\partial x} = 0$ , for  $x = 0, 1$ , for all  $y$ , (2.6 $a$ , $b$ )

In the present study, we use the average-scale equations (2.1) and (2.2) for the basin stability analysis of HRLC in a square enclosure. For this purpose, a fast computational algorithm is necessary for performing the Monte–Carlo simulations over a large number of runs subjected to random initial conditions.

We rewrite the temperature equation based on the departure from the conduction state, i.e.  $\theta_{new} = \theta - (1 - y)$ . This converts the non-homogeneous boundary condition at the bottom surface to a homogeneous one. The dimensionless energy equation then becomes (dropping the subscript for convenience):

$$\frac{\partial \theta}{\partial t} + u \frac{\partial \theta}{\partial x} + v \left( \frac{\partial \theta}{\partial y} - 1 \right) = \nabla^2 \theta, \tag{2.7}$$

where  $\theta$  is now the deviation from the conduction state. This change of variable makes the governing equations suitable for using a fast Poisson solver based on discrete Fourier transforms. For the  $\psi$  field, we use a central finite difference scheme on space derivatives and treat the source term in (2.1) explicitly. The same procedure is used for the temperature field by treating the advective terms in (2.7) explicitly and the diffusion term implicitly.

### 3. Experimental study

# 3.1. Experimental design

For the experimental study, we designed a pseudo-two-dimensional experimental setup using a non-invasive visualization technique based on infrared (IR) thermography. A schematic of the set-up is shown in figure 1. We perform the visualization of the temperature field with a FLIR long-range IR (LWIR) thermal camera within spectral

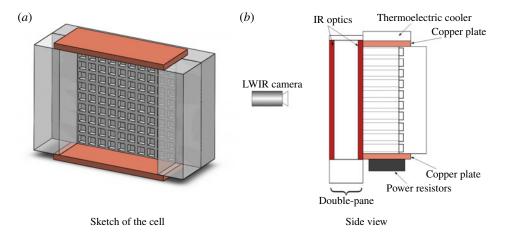
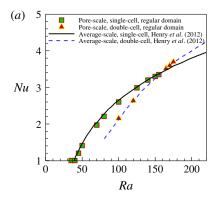


FIGURE 1. Schematic of the experimental convection cell (not to scale); panel (a) shows only the fluid-filled area without the solid square rods, for clarity.

ranges of 7.5 and 13  $\mu m$ . The experimental domain consists of a  $10\times10$  array of acrylic rods and it is filled with 20 cSt silicone oil. The thermal conductivity of the silicone oil and acrylic are 0.142 and 0.19 W  $m^{-1}~K^{-1}$ , respectively. The porosity is 0.5 and the size of the cell is  $45\times45\times10~mm^3$ . The domain is heated from below with power resistors and cooled from the top with a thermoelectric module. Using copper plates with very high thermal conductivity compared to acrylic and silicone oil at the bottom and top boundaries allows us to assume a constant-temperature boundary condition, which was tested continuously with a set of K-type thermocouples attached to both copper plates. Additionally, a PID-based temperature controller is used to control the temperature on the two horizontal plates.

The choice of  $10 \times 10$  array is based on detailed pore-scale numerical simulations over a two-dimensional domain similar to the one shown in figure 1 (Karani & Huber 2017). The pore-scale simulations, which have been conducted with a thermal lattice Boltzmann model (Karani & Huber 2015), show that the average thermal behaviour of a  $10 \times 10$  pore-scale domain is analogous to that of a Darcian homogeneous porous medium and satisfies the assumption of local thermal equilibrium between the solid and fluid phases over the range of values of Rayleigh number considered here (Karani & Huber 2017). Figure 2(a) shows that the average Nusselt number computed from the pore-scale  $10 \times 10$  simulations agrees with the average-scale solution for both single- and double-cell convection modes. Figure 2(b) also shows that increasing the resolution from  $10 \times 10$  to  $20 \times 20$  does not affect the simulated temperature profiles over the domain. We used the same lattice Boltzmann model and calculated the Darcy number of the porous enclosure to be  $Da = K/H^2 = 2.435 \times 10^{-5}$  (Karani & Huber 2017).

In the present pseudo-two-dimensional set-up, we used thick insulating materials at the sidewalls of the porous enclosure. Visualization from the front requires an IR-transparent window while limiting the amount of heat loss from this side. For this purpose, we use an AMTIR (amorphous material transmitting infrared radiation) optic, which has a low thermal conductivity of about 0.25 W m<sup>-1</sup> K<sup>-1</sup>. The window is treated with antireflective (AR) coatings on both sides. In order to further minimize the heat loss from the front, two of these AMTIR optics of 2 mm thickness have been assembled to form a double-pane IR window (figure 1b). The IR camera reads



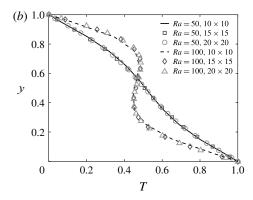


FIGURE 2. (a) Comparison of heat transfer data between pore-scale simulations of  $10 \times 10$  solid blocks (Karani & Huber 2017) and the average-scale solution of Henry *et al.* (2012) for single- and double-cell patterns; (b) horizontally averaged temperatures of the pore-scale simulations for  $10 \times 10$ ,  $15 \times 15$  and  $20 \times 20$  solid blocks.

the temperature field of the outermost layer of the convection cell, which is in contact with the IR optic. This comprises both the fluid phase and the solid blocks. The contact between the square blocks and the IR optic was made with a thin (submillimetre) layer of a thermally conductive paste.

Since the ratio of the depth of the convection cell to its height and width is 4.5 times smaller than the frontal aspect ratio, i.e. 1, we can assume that, for the range of Rayleigh numbers studied experimentally, the effect of the third dimension is relatively negligible. Therefore, we can assume that the flow patterns are mostly two-dimensional. The heat transfer readings presented in the next section confirm this assumption. The amount of heat transfer characterized by the average Nusselt number is calculated from the net electrical power input:

$$Nu = \frac{[\text{net power input}]}{Ak_m(T_H - T_C)/H},$$
(3.1)

where A is the surface area of the bottom hot surface.

### 3.2. Experimental results

We conduct a series of experiments where we ramp up Ra by sequentially increasing the temperature difference between the hot and cold plates and letting the system relax to reach a steady state at each step. In a steady state, we record the average heat flux (Nu) and flow patterns for each experiment. In other words, for each convection case, the initial conditions are always the steady flow reached at the previous Rayleigh number. Figure 3 illustrates the observed steady patterns for several Rayleigh numbers shown as black and white fringes. At Ra = 32, which is below the critical value of  $4\pi^2$ , figure 3(a) shows that heat conduction prevails, i.e. the isotherms are horizontal. The curvature in the lower left part of the isotherms in figure 3(a) is due to a very small gap between the lower left square acrylic rod and the IR optic, resulting in imperfect horizontal isotherms in that region. The maximum Rayleigh number explored is Ra = 221; higher values have been avoided because of the high bottom boundary temperature.

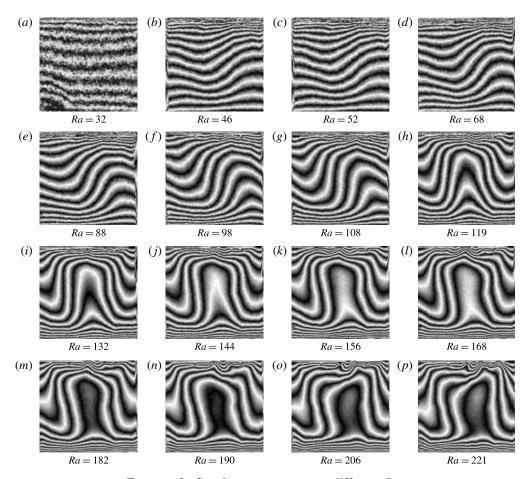


FIGURE 3. Steady-state patterns at different Ra.

Taking a closer look at the steady-state patterns in figure 3 reveals that the stable mode is a single-cell pattern with a counter-clockwise rotation for Ra = 46-108. Then the stable mode switches naturally from single-cell at Ra = 108 to double-cell at Ra = 119, which remains the dominant mode for the rest of the Rayleigh numbers explored. The same behaviour was observed when the Rayleigh number was decreased from Ra = 221 to Ra = 46, with the transition point occurring at exactly the same point and no signs of hysteresis or triple-cell pattern were found.

In order to identify the point of transition more accurately, we applied a smaller heating step at Ra = 108 and recovered a single-cell mode at Ra = 115. A further increase from Ra = 115 to Ra = 119 resulted in the transition from single-cell to double-cell convection. Figure 4 shows snapshots of the reorganization of the convection cells from single- to double-cell during the transition from Ra = 115 to Ra = 119. The step's magnitude of  $\Delta Ra = 4$  was the minimum that could be achieved in the current experimental set-up, and any effort to recover the single-cell mode beyond Ra = 115 led to the transition to the double-cell pattern.

We complemented this series of experiments with a different heating scenario. The goal of this new set of experiments is to verify whether the point of transition is sensitive to the magnitude of the applied thermal loading  $\Delta Ra$ . Figure 5 presents a

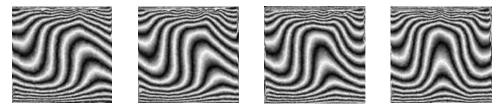


FIGURE 4. Experimental snapshots (IR images) of the transition from single-cell mode at Ra = 115 (leftmost pattern) to double-cell mode at Ra = 119 (rightmost pattern).

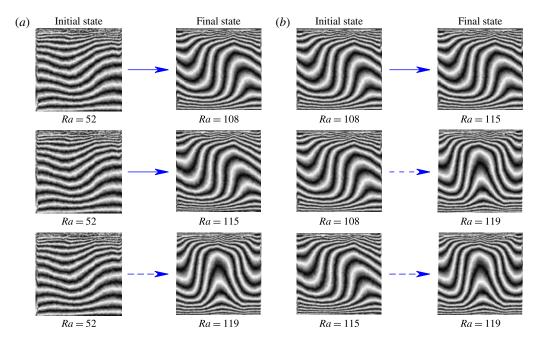


FIGURE 5. Summary of the transitional behaviour from single-cell to double-cell in our experiments: (a) large  $\Delta Ra$ , (b) small  $\Delta Ra$ .

summary of the results for both large and small heating size  $\Delta Ra$ , and reveals that using a large  $\Delta Ra$  and starting off from the steady-state pattern at Ra = 52 leads to a single-cell convection mode at Ra = 108 and 115. The transition to double-cell mode occurs again at Ra = 119, similar to the case with small  $\Delta Ra$  (see figure 5b). The only observed difference in the transitions under small and large thermal loading  $\Delta Ra$  is that the former happens in a significantly shorter time than the latter, i.e. about 3 h compared to about 9 h.

Figure 6 shows a comparison of the correlation of heat transfer data Nu and the thermal forcing Ra in the experiments with those from the numerical solution offered by Henry  $et\ al.\ (2012)$  for HRLC in a 2-D square container. The Ra at which the change in modality of convection is experimentally observed to occur is marked by an arrow. Good agreement is observed between the data points and the average-scale solution of Henry  $et\ al.\ (2012)$ . The main discrepancy occurs at higher Ra values where the increase in the heat loss from the front of the set-up with the double-pane window becomes significant.

### H. Karani and C. Huber

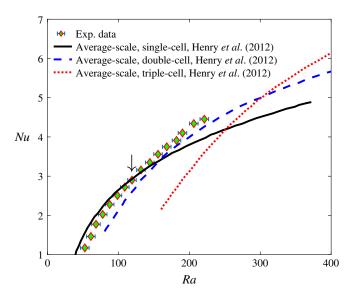


FIGURE 6. *Nu* measured experimentally for single- and double-cell modes. Lines: average-scale solution based on Darcy single-temperature models of Henry *et al.* (2012); symbols: experimental data. The arrow shows the transition point between single-cell and double-cell patterns observed experimentally.

At the experimentally found transition point, the bifurcation analysis of HRLC tells us that both single- and double-cell patterns can coexist (Henry *et al.* 2012). However, the natural transition from single-cell to double-cell mode under different heating scenarios shows that, although both modes are stable, they possess different extents of stability in the face of random perturbations, and this is responsible for the hopping from one stable pattern to another. Therefore, the multiplicity of HRLC calls for a new metric that characterizes the relative stability of different stable patterns. The basin stability analysis of HRLC provides the details of this characteristic in the next section.

# 4. Basin stability analysis of HRLC

We use a basin stability analysis (Menck *et al.* 2013) to find the relative stability of different convective modes when the system is subjected to random perturbations. A basin stability analysis links the volume of the basin of attraction in a multistable system to the likelihood of finding the system in a certain steady state (Menck *et al.* 2013).

The detailed continuum-scale bifurcation analysis of Henry *et al.* (2012) shows that the first four modes in HRLC are stable below Ra = 382.93. In this section, we extend the results of Henry *et al.* (2012) by not only providing the information about the range of existence, but also showing how the basin of attraction of each mode varies with the Rayleigh number, and how this results in different probabilities of occurrence.

To perform the basin stability analysis for HRLC, it is necessary to calculate the basin of attraction for each stable convective mode. A basin of attraction is the set of all points in the phase space, chosen as random initial conditions, that return the system to a specific attractor. In realistic porous media, the factors influencing the final asymptotic stable convective modes may originate from different sources, such

as imperfect boundaries, uncertainties in thermophysical properties, uncertainties in the initial conditions and uncontrolled noise from the environment. In the present study, we focus on the contribution of random initial conditions to the selection of stable modes. As pointed out by Venturi, Wan & Karniadakis (2010), the complete formulation of initial perturbations in real physical systems involves the incorporation of an infinite number of wave modes, which makes the problem computationally prohibitive. Here, since equation (2.1) is a boundary value problem and fluid inertia is negligible, we assume that the initial perturbation applies only to the conduction solution of the temperature field and involves only a finite number n of wave modes, in the following form:

$$\theta_{pert}(x, y, t = 0) = \sum_{k=1}^{n} a_k \cos(k\pi x) \sin(\pi y),$$
 (4.1)

where  $a_k \in [-1, 1]$  is a random variable based on a uniform probability distribution. We consider multiple values for the number of wave modes n to investigate how different modes in the initial perturbation contribute to the asymptotic final stable state within the range of Ra studied here.

The basin stability at a given Rayleigh number is computed using the continuum-scale equations (2.1) and (2.7) with homogeneous boundary conditions and subjected to random initial perturbations defined as in (4.1). We determine the basin stability (or equivalently the probability of occurrence) of each mode by counting its relative proportion of realizations that led to a given cell pattern under steady conditions.

Figures 7–9 show the basin of attraction of different convective modes. In these figures,  $a_1$  to  $a_4$  are the prefactors of the first four wave modes, indicating the relative contribution of each in the initial perturbation field in (4.1). The basins of attraction at Ra = 100 shown in figure 7 clearly illustrate that, although single- and double-cell modes coexist at this Rayleigh number, the first convective mode possesses a larger basin of attraction. However, figure 8 shows how the basin of attraction of the first mode shrinks considerably in size as the Rayleigh number increases from 100 to 150. We observe that for Rayleigh numbers of 100 and 150, only the first and second convectives modes are stable, which is consistent with the bifurcation analysis of Henry *et al.* (2012). Also, the basins of attraction in figures 7 and 8 show a strong dependence of the stable convection mode on the prefactors  $a_1$  and  $a_2$ , and a weak dependence on  $a_3$  and  $a_4$ . This behaviour, however, changes for Ra = 250, where the triple-cell mode emerges, as shown in figure 9, and  $a_3$  impacts the mode selection process.

Figures 7–9 illustrate that the coexistence of the single-, double- and triple-cell modes is accompanied by a large difference in the size of the corresponding basin of attraction, and that the relative size of the basins of attraction is a strong function of the Rayleigh number. We compare the relative size (volume) of the basins of attraction of each mode to the total size of the basin, which provides a measure of the likelihood of finding a convective mode at a certain Rayleigh number (Menck *et al.* 2013).

Figure 10(a) shows the probability of formation of the first and second convection modes based on n = 2 and n = 4 wave modes in (4.1). There is only a slight difference between considering n = 2 and n = 4 in the initial perturbation. In order to show the role of higher-order wave modes, the probability of each mode is shown in figure 10(b) for a wide range of Rayleigh numbers. The figure shows that increasing the number of wave modes from n = 4 to 10 has an insignificant effect on the probability trends. In other words, higher-order wave modes make a smaller

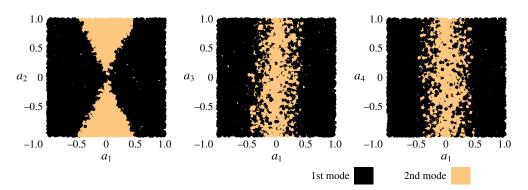


FIGURE 7. Basins of attraction for the first and second convective modes based on the superposition of four modes in the initial perturbation, Ra = 100.

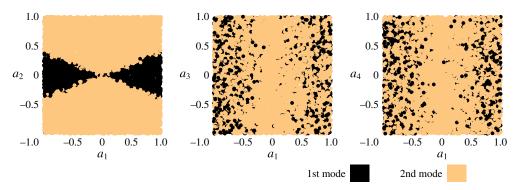


FIGURE 8. Basins of attraction for the first and second convective modes based on the superposition of four modes in the initial perturbation, Ra = 150.

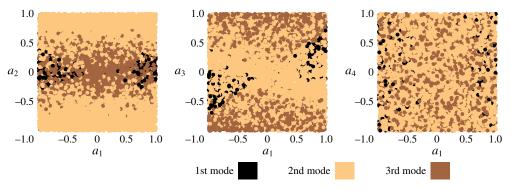


FIGURE 9. Basins of attraction for the first, second and third convective modes based on the superposition of four modes in the initial perturbation, Ra = 250.

contribution to the steady-state stable convection mode over this range of Rayleigh numbers. The overall number of realizations conducted at each Rayleigh number is chosen so as to provide statistically robust results (at least 50 000 realizations, see figure 11).

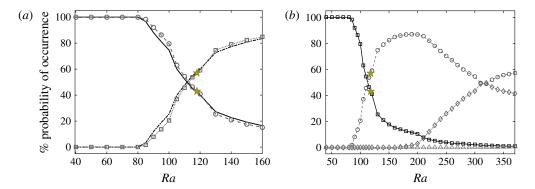


FIGURE 10. Basin stability diagrams. (a) Effect of the first two wave modes (lines) and four wave modes (line-symbols) on the probability of formation; first mode:  $(-, - \circ -)$ , second mode:  $(\cdot -, \cdots \square)$ . (b) Effect of the first four wave modes (lines) and 10 wave modes (symbols) on the probability of formation; first mode:  $(-, \square)$ , second mode:  $(-, \square)$ , third mode:  $(\cdot -, \bigcirc)$ , fourth mode:  $(\cdot \cdot \cdot, \triangle)$ ; The stars show the experimentally observed transition point from single-cell to double-cell pattern.

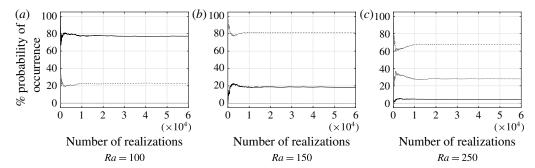


FIGURE 11. Variation of probability of occurrence with the number of realizations; first mode: (-), second mode: (-), third mode:  $(\cdot)$ , fourth mode:  $(\cdot)$ .

The steady bifurcation points for the first four stable convective modes in the basin stability diagram of figure 10(b) agree well with the bifurcation analysis (table 3 in Henry et al. (2012)). However, according to the basin stability diagram of figure 10(b), the domains of coexistence of multiple modes are strongly influenced by their respective basin stability. For example, the probability of finding the first convection mode drops suddenly as the double-cell mode emerges, and in fact it falls below 10% for  $Ra \gtrsim 200$ . At the same time, the formation of double convection becomes more likely, and at  $Ra \sim 112$  it overtakes the single-cell mode and remains stochastically the most probable mode for a wide range of Rayleigh numbers starting from  $Ra \simeq 120$ . Regarding the triple-cell mode, we observe from figure 10(b) that the probability of finding this mode is less than 10% for  $Ra \lesssim 210$ , beyond which it increases considerably up to  $Ra \simeq 315$ . On the other hand, figure 10(b) informs us that the probability of occurrence of the four-cell mode remains below 1% from its steady bifurcation point at  $Ra \simeq 263.7$  (consistent with the bifurcation analysis of Henry et al. (2012)) up to the maximum Rayleigh number studied here. Therefore, the present bifurcation diagram clearly shows that knowledge of just the range of

### H. Karani and C. Huber

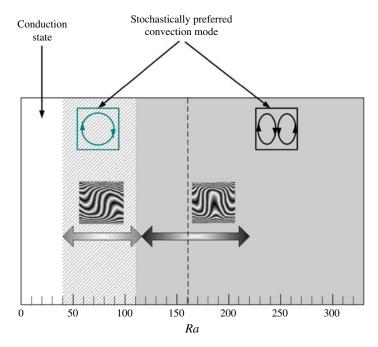


FIGURE 12. Transition points from single-cell to double-cell mode. Horizontal arrows show the experimentally observed patterns; coloured regions indicate the stochastically preferred patterns; the vertical dashed line shows the transition point based on the maximization of heat transfer.

(co)existence of different modes in the multistable HRLC provides only a partial understanding of the complex dynamics of the system.

The star symbols in figure 10(b) show the Rayleigh number where we experimentally observed the transition from single-cell mode to double-cell pattern. The transition point inferred experimentally agrees well with the point where the double-cell mode becomes stochastically preferred over the single-cell mode. For Rayleigh numbers beyond the transition point, we observed experimentally that the double-cell pattern remains the dominant mode, which is consistent with the basin stability diagram.

### 5. Summary

The present study investigates the basin stability analysis of Horton-Rogers-Lapwood convection in porous media. The resulting basin stability diagram provides information on the relative stability of different steady convection modes. The results show that, although different modes coexist over a given range of Rayleigh number, their probability of occurrence varies with Rayleigh number as the relative size of their basin of attraction grows or decreases. Experiments confirm that the transition from a single- to double-cell convection pattern occurs when the sizes of the respective stability basins cross over. The numerical study of Schubert & Straus (1979) confirmed that the preferred convective pattern does not necessarily maximize the heat transfer. The present study further suggests that, under random perturbations/noise, the patterns most likely to emerge are the ones that have the greater basin at that Rayleigh number. Figure 12 compares the transition points from the present basin stability analysis and experimental observations with the patterns that would maximize the

heat transfer (refer to figure caption for details). This comparison confirms that, while the transition point predicted by the basin stability analysis agrees well with the one observed experimentally, the transition point based on the maximization of heat transfer occurs at a higher Rayleigh number. Characterizing the basin of attraction of a desired convective mode and controlling the shape of finite perturbations could potentially allow us to manage the thermal behaviour and to optimize the heat transfer in multistable HRLC.

### References

- BECK, J. L. 1972 Convection in a box of porous material saturated with fluid. *Phys. Fluids* **15** (8), 1377–1383.
- CROSS, M. C. & HOHENBERG, P. C. 1993 Pattern formation outside of equilibrium. *Rev. Mod. Phys.* 65, 851–1112.
- FEUDEL, U. 2008 Complex dynamics in multistable systems. *Intl J. Bifurcation Chaos* 18 (6), 1607–1626.
- HENRY, D., TOUIHRI, R., BOUHLILA, R. & BEN HADID, H. 2012 Multiple flow solutions in buoyancy induced convection in a porous square box. *Water Resour. Res.* 48 (10), w10538.
- HORNE, R. N. 1979 Three-dimensional natural convection in a confined porous medium heated from below. *J. Fluid Mech.* **92**, 751–766.
- HORTON, C. W. & ROGERS, F. T. 1945 Convection currents in a porous medium. *J. Appl. Phys.* **16**, 367–370.
- KARANI, H. & HUBER, C. 2015 Lattice Boltzmann formulation for conjugate heat transfer in heterogeneous media. *Phys. Rev.* E **91**, 023304.
- KARANI, H. & HUBER, C. 2017 Role of thermal disequilibrium on natural convection in porous media: insights from pore-scale study. *Phys. Rev.* E **95**, 033123.
- LAPWOOD, E. R. 1948 Convection of a fluid in a porous medium. *Math. Proc. Camb. Phil. Soc.* 44, 508–521.
- MENCK, P. J., HEITZIG, J., MARWAN, N. & KURTHS, J. 2013 How basin stability complements the linear-stability paradigm. *Nat. Phys.* **9**, 89–92.
- NIELD, D. A. & BEJAN, A. 2013 Convection in Porous Media. Springer.
- RILEY, D. S. & WINTERS, K. H. 1989 Modal exchange mechanisms in Lapwood convection. *J. Fluid Mech.* 204, 325–358.
- SCHUBERT, G. & STRAUS, J. M. 1979 Three-dimensional and multicellular steady and unsteady convection in fluid-saturated porous media at high Rayleigh numbers. J. Fluid Mech. 94, 25–38
- SEZAI, I. 2005 Flow patterns in a fluid-saturated porous cube heated from below. *J. Fluid Mech.* **523**, 393–410.
- STEEN, P. H. 1983 Pattern selection for finite-amplitude convection states in boxes of porous media. J. Fluid Mech. 136, 219–241.
- STRAUS, J. M. & SCHUBERT, G. 1979 Three-dimensional convection in a cubic box of fluid-saturated porous material. *J. Fluid Mech.* **91**, 155–165.
- VENTURI, D., WAN, X. & KARNIADAKIS, G. E. 2010 Stochastic bifurcation analysis of Rayleigh–Bénard convection. *J. Fluid Mech.* **650**, 391–413.
- ZHOU, J. X., ALIYU, M. D. S., AURELL, E. & HUANG, S. 2012 Quasi-potential landscape in complex multi-stable systems. *J. R. Soc. Interface* **9**, 3539–3553.